Tissue Viscoelasticity Quantification using Smartphone Tactile Imaging Probe with an Indenter and Tissue Pitting Recovery Model

Sung In Choi, *Student, IEEE*, Albert Kim, and Chang-Hee Won, *Member, IEEE*

***Abstract*—Viscoelasticity of human tissue often carries important physiological information linking to many fatal diseases, such as heart failure, renal impairment, and liver failure. Fluid retention due to these diseases cause swelling of body parts (edema) and changes the viscoelastic characteristic of the tissue. We hypothesize that the viscoelastic behavior change of the tissue can be estimated by creating and quantifying the pit on the swelled body parts. Here, we present a smartphone tactile imaging probe with an indenter (STIP-I) system that measures the pitting parameters and characterizes the viscoelastic behavior. This system consists of tactile imaging sensing that utilizes a light diffusion in a polydimethylsiloxane (PDMS)-based optical waveguide and a Viscoelastic Pitting Recovery (VPR) computation model. The prototype STIP-I system is tested using edematous tissue phantoms, which show a moderate measurement error of 29.5% for the pitting parameters and excellent performance of 7.60 % error in elastic modulus estimation. The STIP-I system is expected to bring a new approach to understanding viscoelasticity changes due to various diseases.**

***Index Terms*—Body fluid retention, edema severity assessment, smartphone imaging probe, sensing system integration, tactile imaging sensor, tissue viscoelasticity estimation, viscoelastic pitting model and analysis**

I. Introduction

CENTER for Disease Control declares that heart failure is the number one cause of death, with 379,800 deaths in the United States in 2020 [1]. Similarly, 15.0% of the adult population in the United States has chronic kidney disease (CKD) [2], [3]. In many cases of heart or kidney failures, one commonly observed symptom is fluid retention inside the body (i.e., the excessive fluid trapped in body tissue), which is also known as peripheral edema [4]–[9]. While a healthy individual can also experience peripheral edema due to standing or sitting for a long time, over sodium intake, or pregnancy, it can lead to severe complications in heart or kidney disease patients [6], [8]. As such, characterizing edema could provide helpful information for disease progression. For example, studies indicate that chronic peripheral edema is proportional to renal function reduction [6]–[10] and congestive heart failure [9], [11]. Sudden unilateral limb swelling could also imply deep vein thrombosis [6], [7].

Manuscript received April 14, 2022. This work was supported in part by the Temple OVPR 2020-21 Bridge Research Program and the National Science Foundation's ECCS-2114675.

S. I. Choi is with the Electrical and Computer Engineering Department, Temple University, Philadelphia, PA 19122 USA (e-mail: sung.choi@temple.edu).

A. Kim is with the Electrical and Computer Engineering Department, Temple University, Philadelphia, PA 19122 USA (e-mail: albertkim@temple.edu).

C-H. Won is with the Electrical and Computer Engineering Department, Temple University, Philadelphia, PA 19122 USA (e-mail: chang-hee.won@temple.edu).

In the clinic, a physician performs a pitting edema test when excessive fluid retention is observed under body tissue such as the foot or ankle of a patient [7], [8]. A clinician applies pressure to the swollen foot with a finger for a few seconds to examine the lasting indentation (or pit) [7], [8], [12]. Such a test is used to determine the treatment plan, including the administration of diuretic drugs (e.g., furosemide) that help the patient expel excess fluid through urine [9]. The finger pitting test also indicates the viscoelasticity of the swollen tissue. Here, the term viscoelasticity refers to combination of viscosity and elasticity. Viscosity is the amount of resistance to recover the original state from the deformed shape in time; thus, measuring the tissue recovery time from the pitting represents the viscosity [13]–[15]. Elasticity refers to a linear spring force when it deforms and recovers without permanent damage; the tissue pitting depth due to the applied indentation force is therefore associated with elasticity [13]–[15].

However, the finger pitting test lacks the procedural standard [16] and can be a subjective assessment depending on an examiner. Furthermore, the severity metric (Grade I – IV) is vague and cannot be correlated to the disease state. For those reasons, the clinicians do not rely on the pitting test results. Thus, several edematous tissue assessment devices are developed for reliable measurements [16]–[19]. Those devices include an edema depth gauge [16], air compression created pit measurement [17], and direct surface imprinted depth meter [18], [19]. Such apparatuses measure the pitting depth and force applied during the indentation. However, none of these devices can measure the time-dependent viscosity property, which is essential for objective assessment [16], [18], [19].

In this paper, we present a Smartphone Tactile Imaging

Probe with an Indenter (or STIP-I) paired with a Viscoelastic Pitting Recovery (VPR) computation model. The STIP-I system is based on our previous work on the Smartphone-based Compression Induced Sensing (SCIS) system in [20] and tactile imaging systems in [21], [22], which measure the applied force and the corresponding tissue reaction through real-time imaging of interfaced tissue (this technique is called tactile sensing [23], [24]). The STIP-I device interfaces the edematous tissue using an indenter which creates a regulated and repeatable pit. While the indenter interfaces with the tissue, the STIP-I system allows imaging of the deformation and recovery of tissue and finds the pitting parameters: pitting depth, rebound force, and recovery time. The collected images are then further processed via a computational VPR model and obtain the viscoelasticity of the tissue. Lastly, we built a potent diagnosis determinator by comparing the calculated viscoelasticity to the clinical edema severity metric (Grade I – IV). The proposed STIP-I system offers several advantages over the current finger pitting test or other assessment devices, including the precise and objective assessment and tissue visualization during the assessment. Moreover, the use of smartphones increases the accessibility and cost-effectiveness of the system.

The outline of this paper comprises the STIP-I system design, data processing and computation, and experimental results and discussion. This paper also shows the significance of the results of edematous tissue assessment using STIP-I pitting parameters and the VPR model.

II. Sensing System Design

A. System Overview

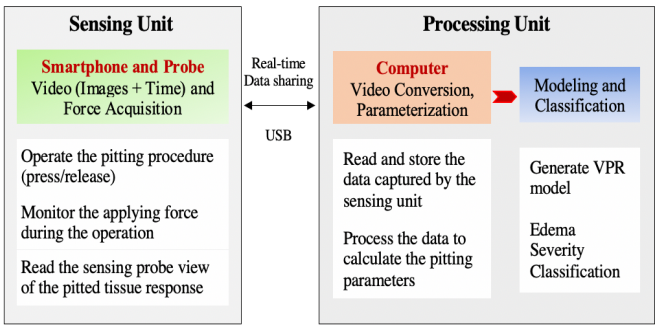

Fig. 1. STIP-I System Functional Block Diagram

Fig. 1 shows the overall architecture of the STIP-I system. Overall, the system can be categorized into two units: sensing and processing units. The sensing unit is the hardware module that enables tactile imaging of the indented tissue (pit), which emulates the finger pitting test. While an attached indenter interfaces the skin, the sensing unit captures a video of pit creation and recovery in real-time. It also reads the applied forces over the course of pitting. The processing unit then retrieves various spatiotemporal information from the video, including pitting depth, rebound force, and recovery time. The data is further processed to compute the viscoelasticity using a viscoelastic pitting recovery (VPR) model, determining the severity.

Fig. 2 illustrates the sensing unit hardware, which consists of three subcomponents: sensing platform, sensing probe, and indenter attachment. The sensing platform shown in Fig. 2 (b) is based on our previously reported Smartphone-based Compression Induced Sensing (SCIS) system [20] that uses a smartphone (as an image sensor and data storage; iPhone6S, Apple Inc.) and control electronics. The control electronics contain a force sensor (FC22, TE Connectivity Inc.), a LED control circuit, and a Bluetooth-enabled microcontroller (Adafruit Feather 32u4 Bluefruit LE, Adafruit Industries), powered by a li-ion battery (803860, PCM/Shenzhen Battery CO., LTD). Fig. 2 (c) shows the sensing probe, a mediator between the smartphone and the indenter. As the indenter creates and releases a pit on the edematous tissue, its distal end also compresses the sensing probe with the same force. In other words, the copy of the pit is imprinted on the sensing probe, which is later captured as a video and processed for viscoelasticity computation. In our case, we used transparent hemispherical polydimethylsiloxane (PDMS) (diameter was 50mm and Young's Modulus of 20 kPa) as a sensing tip. The sensing probe also is an optical waveguide that enables tactile imaging with six white LEDs (λ = 470 nm, LTW-42NC5, LITE-ON Technology Co.) that are placed the outer edge of the sensing probe. The sensing probe is then enclosed by an indenter attachment (Fig. 2 (d)) that holds the indenter and the peripheral fixtures. The indenter has a diameter of 15 mm and a length of 12 mm, which can create an identical pit repeatably.

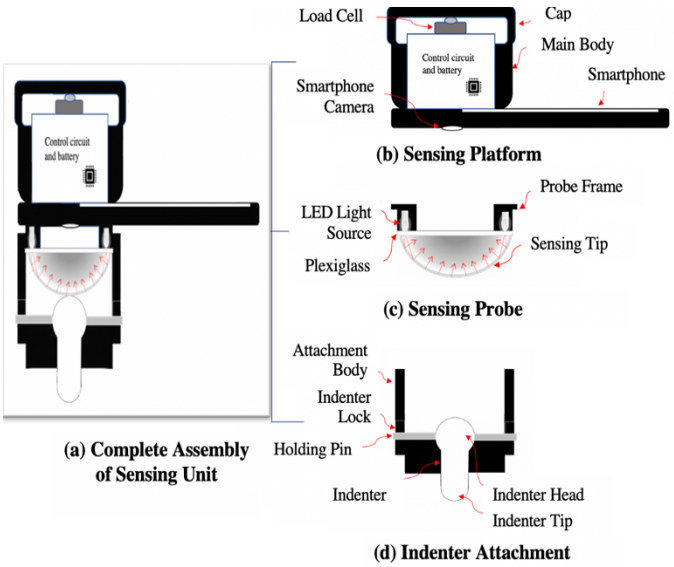

Fig. 2. Design and Subunits of STIP-I Sensing Unit

A part of the sensing unit is a smartphone app that captures the images and reads the force values from the load cell. The app is built for data acquisition using iOS developing environment (Swift 3, XCODE 9.4.1, iOS 10.1). The data collected by the app can be transferred to a personal computer (MacBookPro13,2, Apple Inc.) for post-processing (Processing unit). The processing unit refers to MATLAB software that runs on the computer (MATLAB R2021a). The processing unit converts the recorded video into a series of images with timestamps, computing the pitting parameters and performing the tissue behavior analysis using the VPR model (Fig. 1).

B. Sensing Principle and Operation

concept of the sensing principle. Using six LEDs, light is infused through the sensing probe, inducing reflection on contours (acting as an optical waveguide). As mentioned, the indenter interfaces with the tissue, and it imprints the pit on the sensing probe. It creates a light obstruction on the sensing probe. To the smartphone camera, which directly sits on top of the sensing probe, such light obstruction appears as a circular shape (Fig. 3).

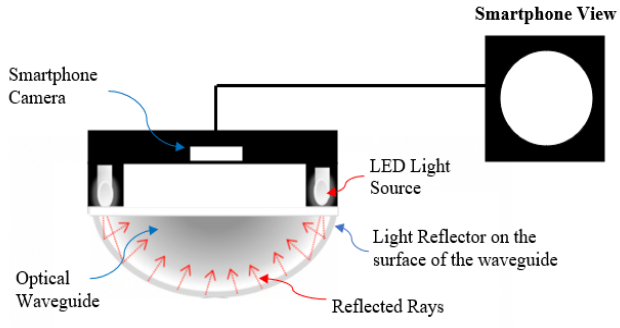

Fig. 3. The schematic of the STIP-I sensing probe and principle

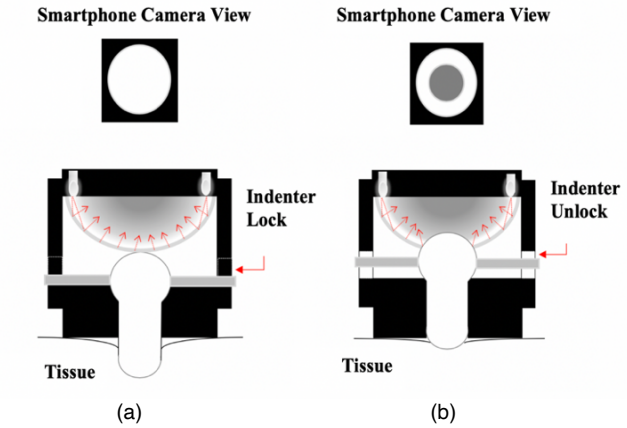

Fig. 4. Sensing principle and operation – (a) Pitting State and (b)Recovery State with the light obstruction due to the soft sensing tip deformation pressed by the rebounding indenter

The operation involves two parts: pit creation and pit recovery as illustrated in Fig. 4. In the pit creation state, the indenter is locked in a place, allowing uniform force application onto the tissue (Fig. 4 (a)). At this phase, the camera image shows an empty white circle. Once the indenter creates a pit, the operation mode is switched to the pit recovery state by unlocking the indenter. The pitted tissue then starts to push back the indenter and imprints the entire course of tissue recovery on the sensing probe in real-time. Since the sensing probe is deformed and the light within the probe is disrupted, it appears as a gray circular pattern on the camera, as shown in Fig. 4 (b). By characterizing this gray circular pattern, it is possible to translate it to the tissue recovery patterns. Such circular patterns are then fed to the VRP model for post-processing.

The sensing principle of the STIP-I tactile probe uses diffused light reflection and light obstruction. Fig. 3 illustrates the

III. Image Processing and Pitting Analysis

A. Image Processing – Thresholding Binary Inverted

The STIP-I system records the tissue deformation and recovery video and stores a series of images over time (frames). The acquired images are processed to generate the pitting parameters. Fig. 5 shows an example image obtained during the operation. The image processing starts by determining the region of interest (ROI) from the raw images. From the raw image (Fig. 5 (a)), the ROI in each image is selected to include the light occluded area that is created by deforming the sensing probe. The original color images are then converted to grayscale images to extract the pixel intensity value. The light occluded area generally shows a low-intensity value compared to the surrounding area after the conversion.

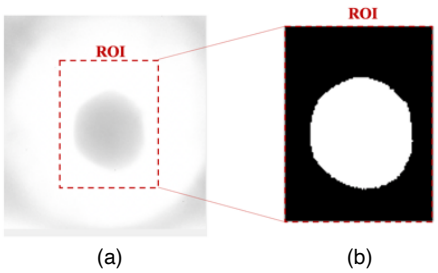

Fig. 5. Image Processing Example – (a) determining ROI (b) thresholding binary inverted image (0 = black, 1 = white, the values are corresponding to the pixel intensity 0=black, 255=white)

Employing the thresholding process, the grayscale image is further processed into the binary image with a black (0) and white (1), depending on the pixel intensity values 0 (black) and 255 (white). The binary value is determined by the following,

$$I_{seg}^{xy} = \begin{cases} 0, & if\ I_g^{xy} > p \\ 1, & otherwise \end{cases} \quad (1)$$

where, I_{seg}^{xy} is the binary pixel value at the location of (x, y) resulted in the threshold binarization, I_g^{xy} is each pixel value at the location (x, y) of the cropped grayscale image, and p is the empirically determined threshold value. In the process of threshold binarization inversion, we assign zero, which corresponds to black, to I_{seg} if the pixel intensity of I_g is greater than the threshold value, p. I_{seg} shows the result of the segmenting light occluded area in the view. The segmented area for the calculation is shown as the white-colored area in Fig. 5 (b). After the image conversion, the area of the light-occluded region is calculated by (2). The sum of all binary image pixels in the ROI area of the segmented k^{th} frame image, $I_{seg,k}^{i,j}$:

$$S_k = \sum_{i}^{i=m} \sum_{j}^{j=n} I_{seg,k}^{i,j} \quad \{i = 1,2, \ldots, m, j = 1,2, \ldots n\}. \quad (2)$$

Each pixel value in the processed image is presented as $I_{seg,k}^{i,j}$ at the pixel coordinate, (i, j). The maximum numbers of i and j

are defined by the size of the window, *m* and *n,* respectively. Later, S_k is converted to the pitting parameters based on the experimentally obtained calibration (see Section IV.B).

$$D_p = l - d_s \,. \tag{3}$$

It is obtained by finding the difference between the total length of the indenter (l = 12 mm) and the depth change, d_s, in the range between 0 and l. The d_s can be retrieved from the S_k as follows,

$$d_s = -\alpha_1 S_0^2 + \alpha_2 S_0 \tag{4}$$

where $\alpha_1$and $\alpha_2$are empirical coefficients determined during the calibration, and S_0 is the initial value of S_k.

During the recovery phase, the pitted tissue pushes the indenter upward and compresses the sensing probe with the rebound force. This force would be directly proportional to the size of the light-occluded pattern in the camera view. The rebound force,

$$F_r = \frac{S_{max} - C_1}{C_2} \tag{5}$$

is also related to the S_k as the area with respect to the mechanical property of the sensing probe. In (5), S_{max} is the maximum S_k and the C_1 and C_2 are empirically determined mechanical properties of the sensing tip.

The recovery time, *Tr*, is obtained by identifying the time values at the recovery state starting and ending. Owing to the settling time concept of in control systems analysis for the step input response [25], the output variation of a handheld device could be dramatically reduced. Equation (6) shows the tissue recovery time, T_r, which is the difference between the settling time, T_s, and the initial time, T_0. T_s is measured when S_k reaches 98.0% of S_{max}. T_0 is the time of S_0 when the tissue starts to recover.

$$T_r = T_s - T_0 \,. \tag{6}$$

Note that the recovery time is a crucial element in determining the viscosity of tissue as it causes a time delay in tissue reshaping.

C. Viscoelastic Pitting Recovery (VPR) Model

The Maxwell model, the Kelvin-Voigt model, and the standard linear solid (SLS) model are the most used viscoelastic models in theoretical mechanical modeling [26]–[29]. The Maxell model represents the tissue as a viscous damper (η_{tss}) and an elastic spring (E_{tss}) coupled in series [26]–[28]. The Kelvin-Voigt model has a parallel structure of a viscous component and an elastic component, and the SLS model is a hybrid of the Maxell and Kelvin-Voigt models [26]. Due to the presence of a transition state, which is anelastic behavior not shown in the Maxwell model, the Kelvin and SLS models are more appropriate for describing tissue viscoelasticity [27], [30]. In our VPR model design, the Kelvin-Voigt model (Fig. 6) is used since its strain recovery state is better matched with that of the pitting recovery condition. Combined, the Kelvin-Voigt model describes the viscoelastic behaviors under mechanical loading (pit) and unloading (recovery). The gradual deformation and recovery behaviors of tissue are expressed in terms of stress and strain in the Kevin-Voigt model. As such, we utilize the recovery behavior of tissue at the unloading state to characterize the pitting recovery state.

B. Pitting Parameters Analysis

The pitting parameters, i.e., pitting depth (D_p), rebound force (F_r), and recovery time (T_r) are derived from S_k. First the S_k is calibrated against physical measurements. The pitting depth is:

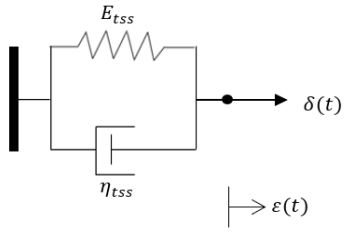

Fig. 6. Kelvin-Voigt model (parallel arrangement) of tissue

To build a viscoelastic behavior model of tissue, the ratio of elasticity to viscosity needs to be determined in the form of time-dependent characteristics [13], [26], [29]. Thus, we calculate the elasticity and viscosity of the tissue using the pitting parameters, i.e., pitting depth D_p, rebound force F_r, and recovery time, T_r.

1) *Elasticity Computation*

Elasticity is defined as the stress over the strain. The most elasticity measurements perform on the material based on the uniaxial and uniform stress (extension or compression). However, it does not suitable for living tissue. Thus, the elasticity estimation based on the indentation presented in [31], [32],

$$E_{tss} = \frac{3}{\pi^2 R} \cdot \frac{F_a}{D_p} \tag{7}$$

is used where E_{tss} is the tissue elasticity, which is proportional to the ratio of applied force, F_a, and the pitting depth, D_p. The tissue interface is caused by the indenter, whose radius is R.

2) *Viscosity Computation*

The viscosity is the internal resistance to the flow of the shape [13]–[15]. The amount of resistance in the viscoelastic material can be determined by measuring the time delay for the complete shape transition. The time delay in the Kelvin-Voigt model is defined as retardation time, which is determined by the ratio of viscosity, η, over the elasticity, E [26], [33]. In our case, the tissue viscosity is unknown, and it can be determined by utilizing the relationship in the time delay, as shown in (8).

$$\eta_{tss} = E_{tss} \cdot T_r \tag{8}$$

The tissue viscosity, η_{tss}, is calculated by the product of the recovery time, T_r, and the tissue elasticity, E_{tss}. Note that viscosity used in this method is not absolute tissue viscosity but

rather a relative value indicating the viscous component of tissue.

3) Viscoelastic Pitting Recovery (VPR) Model

Combining elasticity and viscosity computation, the VPR is built based on the Kelvin-Voigt model and the constitutive law in the standard form [15], [26]. The applied stress, $\sigma(t)$, is shown as follows,

$$\sigma(t) = E\varepsilon(t) + \eta\left(\frac{d\varepsilon(t)}{dt}\right). \quad (9)$$

We are looking for the depth change in the pitted tissue. Thus, we assume that the strain is the ratio of depth change, $D_\varepsilon(t)$ over the initial depth, D_i. We assume that D_i is unity because we are looking for depth change per unit depth. The pit recovery starts where the depth, $D_\varepsilon(0) = D_p$, and the stress σ becomes zero, thus we obtain the following equation from (9),

$$D_\varepsilon(t) = D_p e^{-\left(E_{tss}/\eta_{tss}\right)t} \tag{10}$$

where D_p is the maximum pitting depth at F_a, E_{tss} is tissue elasticity, and η_{tss} is tissue viscosity in our application. Equation (10) is the VPR model, the tissue depth change model in terms of elasticity and viscosity.

IV. Experimental Results

A. Edematous Tissue Phantom

Edematous tissue phantoms made of soft elastomer (Life form Pitting Edema Trainer, Nasco) were utilized to validate the STIP-I functionality and the proposed VPR model. This commercial training tissue phantom mimics clinically defined edema severity grades (I to IVs); A higher grade means severe edema as defined in [34]. Prior to the experiment, the mechanical properties of tissue phantoms were measured using a universal mechanical testing machine (5944B12032, Instron). Young's Modulus of the tissue phantom exhibited 355.59 ± 2.17 kPa for Grade I; 266.37 ± 0.62 kPa for Grade II; 221.35 ± 0.27 kPa for Grade III, and 185.91 ± 0.60 kPa for Grade IV. The dimension of each phantom was 56 × 87 × 18 mm^3.

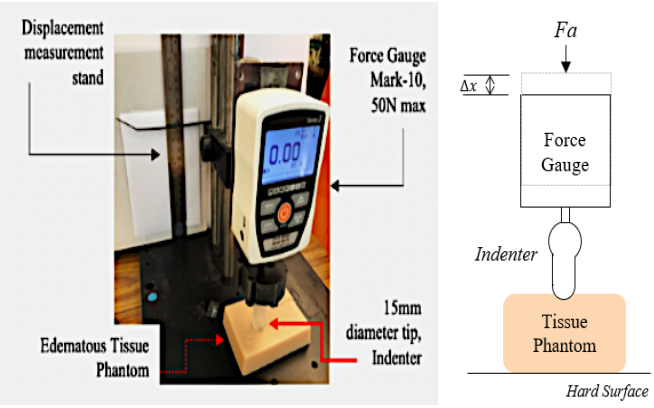

(a) (b)

Fig. 7. Direct Measurement Experiment Setup (a)Experiment Setup and Components, (b) Tissue Phantom Direct Measurement

Fig. 7 shows the experimental setup for the direct measurements. While a force gauge (Force Gauge M3-10, 50N max, Mark-10 Corporation, NY) with an indenter interfaces the tissue phantom, the vertical movements are measured using a ruler (Fig. 7). The measured force through the force gauge defines the STIP-I operating force range, while the measured pitting depth is used for validation in the following section. The result of pitting depth change corresponding to the applied forces to the tissue phantoms is shown in Fig. 8. The phantom with a lower Young's Modulus value (higher grade) had more depth change when applying the same amount of force.

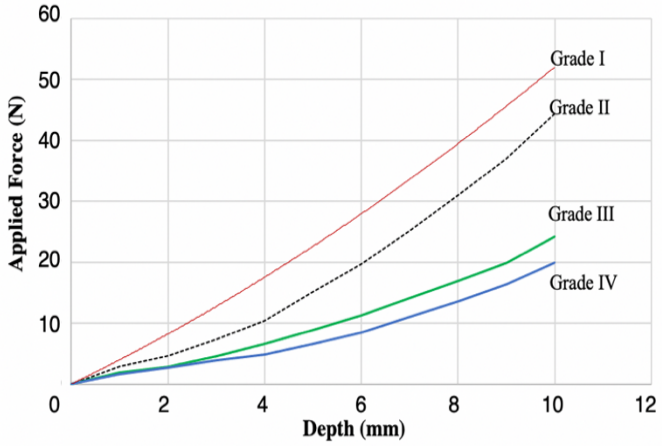

Fig. 8. Direct pitting measurement results for varying applied force

B. Pitting Parameter Acquisition using STIP-I

As described above, the STIP-I system was hardwired to a personal computer for complete viscoelasticity computation. Fig. 9 shows the entire system, including the STIP-I system on a tissue phantom and a laptop. The STIP-I video was recorded for 120 seconds long during a 15-sec pitting and a 105-sec recovery.

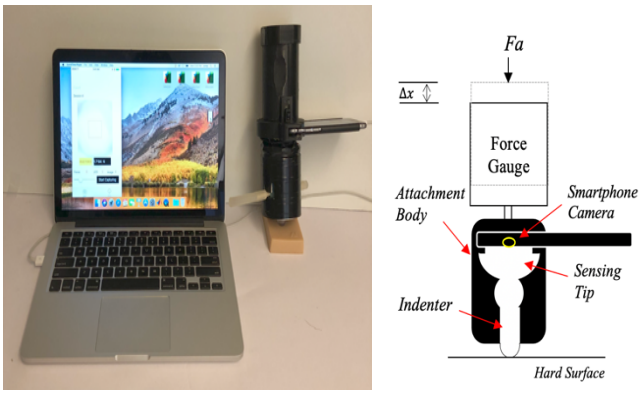

(a) (b)

Fig. 9. STIP-I Measurement experiment setup (a) STIP-I data acquisition (b) direct measurement

Calibration was performed using the experimental setup depicted in Fig. 9 (b). The calibration procedure established the relationship of the S_k (sum of pixels) changes in the images with the applied force to the sensing probe. The size of the segmented area in the image was dictated by externally applied force as the indenter generates the counterforce to the sensing probe due to the mechanical properties of the tissue phantom. The calibration also determined the relationship between the segmented area and the displacement of the indenter, which is the critical factor for computing the pitting parameters.

After the calibration, the mechanical properties of four different tissue phantoms representing clinical edema grades were measured using the STIP-I system. The five trials were executed for each phantom. The applied pitting force was maintained at 16 ± 1.5 N, and images were captured every 0.017 sec (60 FPS). The total duration of each measurement was up to 120 sec: 15 sec for creating pitting and up to 105 sec

for monitoring the total recovery. From the initial testing, we optimized operation time.

TABLE I
VERIFICATION RESULT OF PITTING PARAMETERS

Grade	Pitting Depth (mm)		Rebounding Force (N)		Recovery Time (sec)	
	Ground Truth	STIP-I	Ground Truth	STIP-I	Ground Truth	STIP-I
I	3.65	3.98	7.54	7.26	8.03	2.19
II	5.16	4.74	6.08	6.22	11.5	8.95
III	7.84	6.79	4.92	5.34	17.0	27.5
IV	9.02	7.63	4.21	4.75	19.8	44.4
Avg. Error (%)	11.50		6.84		70.0	

Pitting parameters (D_p, F_r, and T_r, as discussed in Section III.B) were computed using the S_k values and compared with the direct measurements (i.e., ground-truth) (Section IV. A). Table I summarizes the results. The analyzed pitting depth, D_p, resulted in 11.5% of the average error for all four grades. The rebound force, F_r, was comparable with the directly measured rebound force. The F_r showed an excellent agreement with a 6.84% error. The recovery time, T_r, measured by STIP-I, was also compared with that of the finger pitting test. Note that T_r was captured when the S_k reached 98.0% of its maximum. The results showed a high error of 70.0% due to unreliable manual measurements (human error).

C. Viscoelastic Pitting Recovery Model

1) Elasticity and Viscosity

The estimated elasticity values were well correlated with the measured mechanical properties of the tissue phantom, summarized in Table II. In comparison, the overall error was 7.60% as compared to the ground truth. The viscosity, however, showed a high error of 69.0%. This high error is mainly due to the measurement method – we used a stopwatch to obtain the recovery time, which is how the clinicians assess the edematous tissue. Despite the high error, especially for Grade III and IV tissue phantom, the computed T_r strongly correlates to the edematous grade.

TABLE II
RESULT OF ELASTICITY AND VISCOSITY CALCULATION

Grade	Elasticity, E_{tss} (kPa)		Viscosity, η_{tss} (N·s/mm^2)	
	Ground Truth	STIP-I	Ground Truth	STIP-I
I	355.59	376.37	2.86	0.82
II	266.37	316.02	3.05	2.83
III	221.35	220.61	3.76	6.08
IV	185.91	196.32	3.69	8.70
Avg. Error (%)	7.60		69.0	

2) VPR Model and Edema Severity Classification

Viscoelastic characteristics of the tissue govern the recovery patterns of the pitting depth ($D_\varepsilon(t)$) as described in (10)). Fig. 10 is a computed VRP model based on (10) and measured data in Table II. The model could indicate important facts regarding each edema grade: the elasticity and viscosity changes, the maximum pitting depth, the recovery speed. Grade I edema, for example, had the least pitting depth and the fastest recovery time due to high elasticity and low viscosity.

The clinical edema categorization for the severe and mild cases declares edema grade III and above are severe [34]. Thus, identifying the time window that shows the most significant difference between grades II and III in the VPR model (Fig. 10) can be used for classifying the edema severity. Furthermore, a clear threshold between mild and severe edema and its optimal time window is needed.

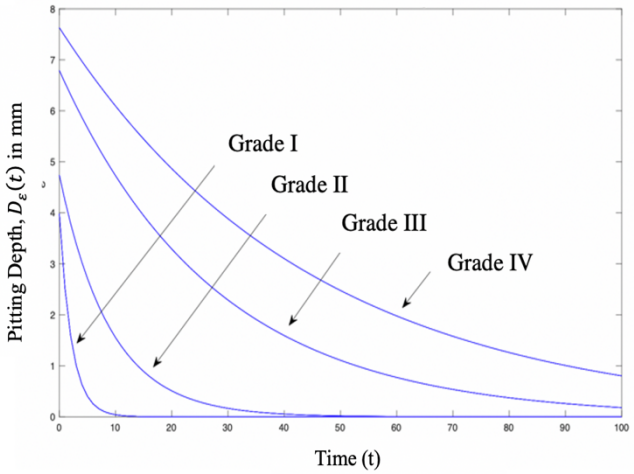

Fig. 10. VPR model for four grades of edematous tissue phantoms

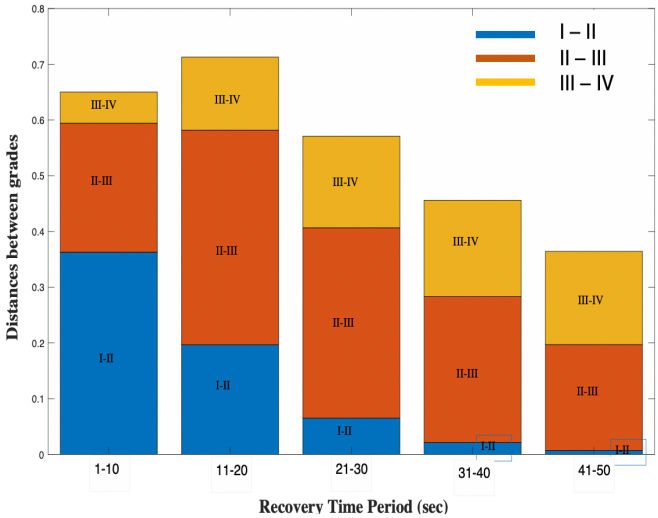

Fig. 11. Average distances of each 10s frame in the 50 sec (1sec – 50 sec) between grades I-II (blue), II-III (orange), and III-IV (yellow)

To identify the threshold value, we first normalized the pitting depth ($D_\varepsilon(t)$) of each edema grade with the maximum pitting depth as 1 and the complete recovery as 0. To obtain the most severity-relevant time window, we identified the most significant depth difference between Grade II and III concerning the recovery time (Fig. 11). For this, the time

window interval was set to 10-sec and the average differences in the pitting depth between each grade were calculated. In our case, we identified the time window of 11 - 20 sec as an edema severity determinant.

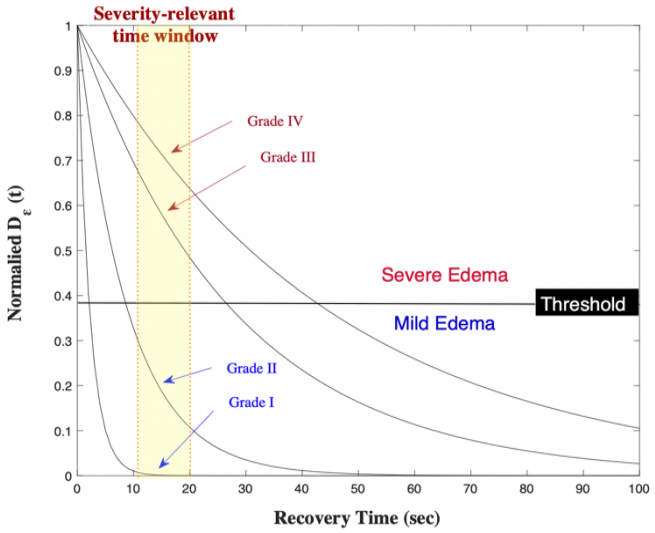

Fig. 12. Edema severity classification using normalized VPR models

We then set the mid-point of the $D_\varepsilon(t)$ as the threshold, which determines mild or severe edema. The example of thresholding is shown in Fig. 12, which is the normalized Fig. 10 with the threshold line. The result shows that tissue with severe edema has a pitting depth less than 62.0% from the maximum during recovery time between 11 and 20 sec.

V. Discussion

Most existing tactile sensors use highly sensitive pressure sensors to quantify the direct touch sensation. However, direct contact-based tactile sensing requires complicated sensing material and algorithms, as discussed in [23], [24]. Moreover, typical tactile sensors usually only detect pressure. Our system also uses tactile sensing combined with imaging via the direct contact method. However, our sensing system can detect the pressure along with the chronological and objective recovery behavior of the pressure applied to tissue, which is needed for tissue viscoelasticity assessment. By utilizing STIP-I, we can read the parameters and time values to quantify the tissue viscoelasticity.

STIP-I measured the pitting depth of the edematous tissue with an error of 11.5% and the rebound force with an error of 6.84%. The errors occurred as a result of the force variation during the operation. The STIP-I operation accepts the range of applying force in 9.38% (16 ± 1.5 *N*) variation. Thus, we could consider the reading errors are within the acceptable range. It is, in general, one of the constraints of a handheld device. The recovery time with a 70.0% measurement error, on the other hand, was much larger than the other measurement errors. It was mainly due to the difference in the full recovery and measurement standard between STIP-I and human testing; the observer decides full recovery when the pitted area returns to its previous state as visibly detectable without a time constraint. Nevertheless, we could optimize the STIP-I procedure to examine the data regarding the pit recovery in a set time frame until the initial condition is restored. To resolve the issue, further improvement in the design of the probe and operational procedure will be needed.

The VPR model could classify edema severity even with a limited set of data and a small number of tissue phantom samples. Despite the limitations, we proposed the edema severity classification based on the viscoelastic measurements. By implementing the pitting depth threshold within the severity-relevant time window, we successfully identified the severe edema grades (Grade III and IV) from the mild cases. Extracellular fluid rising rates for each edema grade were defined as approximately 30.0% for Grade I, 45.0% for Grade II, 60.0% for Grade III, and 80.0% for Grade IV in the interstitial pressure study [35], [36]. The fluid increasing rate has a strong correlation with the pitting recovery speed shown in the VPR model (high as $r = -0.97175$). This finding provides the potential of the VPR model to estimate the fluid retention level in tissue for our future work.

VI. Conclusion

In this paper, we presented the Viscoelastic Pitting Recovery (VPR) model to evaluate the mechanical property change of an edematous tissue due to the abnormal increase of fluid. To construct the accurate model, we designed and developed the noble pitting parameter measuring system, Smartphone Imaging Probe – Indenter (STIP-I) system. STIP-I system produces pitting parameters (pitting depth, rebounding force, and recovery time). The experiment to estimate the pitting parameters using the edematous tissue phantoms (four types) resulted in a moderate error and the elasticity calculation using the parameters resulted in an excellent agreement with the gold standard. Also, the calculated viscosity based on the STIP-I measurements showed a high potential to estimate the retained fluid amount change in tissue. We were able to build the VPR model using the calculated elasticity and viscosity of the tissue phantoms and utilize the model to visualize the pitting recovery state of each tissue in time. The edema severity of the phantom tissues was successfully classified using the VPR models with the recovery percentage thresholding. STIP-I showed the ability to accurately quantify and characterize edema, which will be utilized to diagnose and treat diseases that cause edema.

References

[1] Centers for Disease Control and Prevention, “Heart Failure,” 2020. Accessed: Feb 20, 2021. [Online]. Available: https://www.cdc.gov/heartdisease/heart_failure.htm

[2] Centers for Disease Control and Prevention, “Chronic Kidney Disease in the United States, 2019,” 2019. Accessed: Feb 20, 2021, [Online]. Available: https://www.cdc.gov/kidneydisease/publications-resources/2019-national-facts.html

[3] S. L. Murphy, J. Q. Xu, K. D. Kochanek, E. Arias, and B. Tejada-Vera, “Deaths: Final data for 2018,” National Vital Statistics Reports, Hyattsville, MD Natl. Cent. Heal. Stat., vol. 69, no. 13, 2021.

[4] E. Braunwald & J. Loscalzo, “Edema,” in *Harrison's Principles of Internal Medicine*, Kasper D, & Fauci A, & Hauser S, & Longo D, & Jameson J, & Loscalzo J(Eds.), 19th ed. New York, NY, USA: McGraw-Hill, 2014. [Online]. Available: https://accessmedicine.mhmedical.com/content.aspx?bookid=1130&sectionid=79725994

[5] T. Davenport, K. Kulig, C. Sebelski, J. Gordon, and H. Watts, “Description of Conditions That May Lead to Edema,” in *Diagnosis for Physical Therapists,* 1st ed. Stockton, CA, USA: F.A. Davis Company, 2013. [Online]. Available: https://www-r2library-com.libproxy.temple.

edu/Resource/Title/0803615280/ch0038s3513
[6] L. Kennedy-Malone and L. Martin-Plank, “Symtoms and Syndromes – Peripheral Edema,” in Advanced practice nursing in the care of older adults, 2nd ed. Philadelphia, PA: F.A. Davis Company, 2018, pp. 74-76.
[7] A. P. Gasparis, P. S. Kim, S. M. Dean, N. M. Khilnani, and N. Labropoulos, “Diagnostic approach to lower limb edema,” *Phlebology*, vol. 35, no. 9, pp. 650–655, Jul. 2020.
[8] D. Camp-Sorrell and R. Zollman, Eds., “Peripheral Edema,’ in *Clinical Manual for the Oncology Advanced Practice Nurse*, 3rd ed. Pittsburgh, PA: Oncology Nursing Society, 2014, pp. 319-326.
[9] Mayo Clinic, “Edema: Diagnosis and Treatment.” Mayo Foundation for Medical Education and Research, Accessed: Mar. 14, 2022. [Online]. Available: https://www.mayoclinic.org/diseases-conditions/edema/diagnosis-treatment/drc-20366532
[10] L. M. Ebah *et al.,* “Subcutaneous interstitial pressure and volume characteristics in renal impairment associated with edema,” *Kidney Int.*, vol. 84, no. 5, pp. 980–988, Nov. 2013.
[11] “Causes and signs of edema,” InformedHealth.org, Cologne, Germany: Institute for Quality and Efficiency in Health Care. [Updated: Dec 30, 2016]. [Online]. Available: https://www.ncbi.nlm.nih.gov/books/NBK279409/
[12] H. Kogo, T. Higashi, and J. Murata, “Reliability of a new practical evaluation method for pitting edema based on the depth of the surface imprint,” *J. Phys. Ther. Sci*., vol. 27, no. 6, pp. 1735–1738, Jun. 2015.
[13] H. T. Banks, S. Hu, and Z. R. Kenz, “A brief review of elasticity and viscoelasticity for solids,” *Adv. Appl. Math. Mech*., vol. 3, no. 1, pp. 1–51, Feb. 2011.
[14] R. Lakes, *Viscoelastic Materials*. New York, NY, USA: Cambridge University Press, 2009, pp. 1–12.
[15] S. F. Duffy, “Linear viscoelasticity mechanical (rheological) models,” Cleveland, OH, USA: Cleveland State University, 2010. [Online]. Available: https://academic.csuohio.edu/duffy_s/Linear_Visco.pdf.
[16] K. G. Brodowicz, K. McNaughton, N. Uemura, G. Meininger, C. J. Girman, and S. H. Yale, “Reliability and feasibility of methods to quantitatively assess peripheral edema,” *Clin. Med. Res.*, vol. 7, no. 1–2, pp. 21–31, Jun. 2009.
[17] K. Williams, M. Han, S. Hardin, S. George, and J. Yao, “AERO: An Objective Peripheral Edema Measurement Device,” in *40th Annu. Int. Conf. IEEE Eng. Med. Biol. Soc.*, 2018, pp. 5914–5917.
[18] S. LeGare, E. Hall, R. Horwitz, C. Gammal, R. Dunn, and Y. Mendelson, “A device to assess the severity of peripheral edema,” *IEEE 33rd Annu. Northeast Bioeng. Conf.*, 2007, pp. 257–258.
[19] H. Kogo, J. Murata, S. Murata, and T. Higashi, “Validity of a new quantitative evaluation method that uses the depth of the surface imprint as an indicator for pitting edema,” *PLoS One*, vol. 12, no. 1, pp. 1–10, Jan. 2017.
[20] S. Choi, V. Oleksyuk, D. Caroline, S. Pascarella, R. Kendzierski, and C.-H. Won, “Breast Tumor Malignancy Classification using Smartphone Compression-induced Sensing System and Deformation Index Ratio,” in *42nd Annu. Int. Conf. IEEE Eng. Med. Biol. Soc.*, Montr. QC, Canada, 2020, pp. 6082–6085.
[21] J.-H. Lee and C.-H. Won, “High-resolution tactile imaging sensor using total internal reflection and nonrigid pattern matching algorithm,” *IEEE Sensors J.*, vol. 11, no. 9, pp. 2084–2093, Sep. 2011.
[22] V. Oleksyuk, R. Rajan, F. Saleheen, D. F. Caroline, S. Pascarella, and C.-H. Won, “Risk score based pre-screening of breast tumor using compression induced sensing system,” *IEEE Sensors J.,* vol. 18, no. 10, pp. 4038–4045, May 2018.
[23] C.-H. Won, J.-H. Lee, and F. Saleheen, “Tactile Sensing Systems for Tumor Characterization: A Review,” *IEEE Sens. J.*, vol. 21, no. 11, pp. 12578–12588, May 2021.
[24] X. Sun *et al.*, "Recent Applications of Different Microstructure Designs in High Performance Tactile Sensors: A Review," *IEEE Sensors J.*, vol. 21, no. 9, pp. 10291–10303, Feb. 2021.
[25] N. Nise, “Time Response,” in *Control Systems Engineering*. Hoboken, New Jersey: Wiley, 2011, pp. 157-234.
[26] P. Kelly, “Solid mechanics part I: An introduction to solid mechanics: 10_Viscoelasticity,” Mechanical Engineering, The University of Auckland, Auckland, New Zealand, 2015. [Online]. Available: http://homepages.engineering.auckland.ac.nz/~pkel015/SolidMechanicsBooks/Part_I/BookSM_Part_I/10_Viscoelasticity/10_Viscoelasticity_Complete.pdf.
[27] J. Yao, E. M. B. Weaver, B. D. Langley, S. M. George, and S. R. Hardin, “Monitoring peripheral edema of heart failure patients at home: Device, algorithm, and clinic study,” in *Annu. Int. Conf. IEEE Eng. Med. Biol. Soc. Annu. Int. Conf.*, 2017, pp. 4074–4077.
[28] B. Belmont, R. E. Dodde, and A. J. Shih, “Impedance of tissue-mimicking phantom material under compression,” *J. Electr. Bioimpedance*, vol. 4, pp. 2–12, Feb. 2013.
[29] K. S. Cho, “Theory of Linear Viscoelasticity,” in *Viscoelasticity of Polymers*. Springer Series in Materials Science, vol. 241, Daegu, Republic of Korea: Springer, Dordrecht, 2016, pp. 285-359.
[30] N. Özkaya and M. Nordin, "Mechanical Properties of Biological Tissues," in *Fundamentals of Biomechanics.* New York, NY, USA: Springer,1999, pp. 195-218.
[31] V. Egorov, S. Tsyuryupa, S. Kanilo, M. Kogit, and A. Srvazyan, “Soft tissue elastometer,” NIH Public Access. Med. Eng. Phys., vol. 30, no. 2, pp. 206–212, 2008.
[32] S. Timoshenko and J. N. Goodier, Theory of elasticity. New York: McGraw-Hill Book Company, 1951.
[33] W. N. Findley, J. S. Lai, and K. Onaran, Creep and Relaxation of Nonlinear Viscoelastic Materials - With an Introduction to Linear Viscoelasticity. Dover Publications, 1976.
[34] D. Shelledy, and J. Peters, “Physical Assessment” in Extremities. *Respiratory Care: Patient Assessment and Care Plan Development*, 1st ed. Burlington, MA, USA: Jones & Bartlett Learning, 2016. [Online]. Available: https://www-r2library-com.libproxy.temple.edu/Resource/Title/1449672442/ch0005s0236
[35] A. C. Guyton, H. J. Granger, and A. E. Taylor, “Interstitial fluid pressure,” *Physiol. Rev.*, vol. 51, no. 3, pp. 527–563, Jul. 1971.
[36] A. C. Guyton, “Interstitial Fluid Pressure. II. Pressure-Volume Curves of Interstitial,” *Circ. Res.*, vol. 16, pp. 452–460, May 1965.

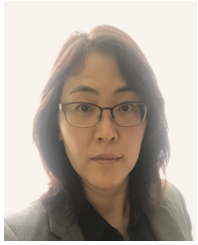

Sung In Choi (M’12) was born in Seoul, South Korea in 1978. She received her B.S. and M.S. degrees in electrical and computer engineering from Temple University, Philadelphia, PA, USA in 2013. Currently, she is pursuing the Ph.D. degree in electrical and computer engineering at Temple University.

From 2013 to 2022, she was a Research Assistant with the Control, Sensor, Network, and Perception (CSNAP) Laboratory. Her research interests include the development of personalized biomedical sensing systems using optical and tactile sensors and risk estimation modeling to detect the early stage of breast cancer and cardiovascular disease based on tissue mechanical property estimation.

Albert Kim received his doctoral degree in electrical and computer engineering from Purdue University in 2015. From 2015 to 2017, he was an R&D engineer at Intel Corp. Since 2017, he has been with the Department of Electrical and Computer Engineering of Temple University as an Assistant Professor.

He is the author of more than 70 articles and holds two patents. His research interests include Acousto-Bioelectronics, biomedical microdevices, implantable wireless microsystems, and biosensors. His research is funded by National Science Foundation (NSF).

Chang-hee Won, (M’87) is a Professor of the Electrical and Computer Engineering Department and the director of the Control, Sensor, Network, and Perception (CSNAP) Laboratory at Temple University.

Before coming to academia, he worked at Electronics and Telecommunications Research Institute (ETRI) as a senior research engineer. Currently, he is actively guiding various research projects funded by the National Science Foundation, Pennsylvania Department of Health, and Department of Defense.

Dr. Won is an associate editor of IEEE Sensors Journal. His research interests include tactile sensors, stochastic optimal control theory, spectral sensors, and dynamic interrogation systems.